Electrical Impedance Tomography
in Three Dimensions

J. Goble *, M. Cheney [†] and D. Isaacson [†*]

Rensselaer Polytechnic Institute, Troy NY 12180

6 October 1992

Abstract

An algorithm is developed for electrical impedance tomography (EIT) of three–dimensional volumes using multi–planar electrode arrays. This algorithm is based upon the method of least squares, and uses one step of Newton's method to estimate the conductivity distribution inside the volume using electrical measurements made on the boundary.

An implementation of the algorithm for right cylindrical volumes is described. This computer code, called *N3D*, permits reconstructions with up to 2016 degrees of freedom. The code uses an initial guess consisting of a uniform conductivity, allowing many of the computations to be done analytically.

Although the code does not reconstruct the conductivity distribution accurately (unless it differs very little from a constant,) it does yield useful images at reasonable computational cost. The algorithm is demonstrated using three–dimensional resistivity distributions reconstructed from experimental data.

Introduction

The inverse problem in Electrical Impedance Tomography (EIT) considers the reconstruction of the electrical characteristics inside the body from measurements made on the skin.

---
*Department of Computer Science
[†]Department of Mathematical Sciences

Material	Resistivity (ρ) ohm-cm
Urine	30
Plasma	63
Cerebrospinal fluid	65
Blood	150
Skeletal muscle	300
Cardiac muscle	750
Lung	1275
Fat	2500
Copper	1.724×10^{-6}

Table 1: Typical Tissue Resistivity Values

Although superficially similar, this task is fundamentally different from that encountered in X-ray Computed Tomography(CT) or Positron Emission Tomography(PET), where the photon paths through tissue are essentially straight lines. In contrast, the current paths in EIT are functions of the unknown conductivity distribution, and the reconstruction problem is highly non-linear. We focus here on biomedical applications of EIT, but note that the technique has been used in geophysical exploration and may have important uses in non-destructive testing, and in the monitoring of industrial processes such as solidification and multi-phase flow.

Biological Basis of the EIT Signal

Biological tissues contain free charge carriers that permit them to act as (relatively poor) electrical conductors. This ability to conduct varies substantially among various types of tissue: some typical values of resistivity for tissues of interest have been tabulated [Baker, 1989] and are presented as Table 1. For reference, the resistivity of pure copper is included. The goal of EIT is to compute and display the spatial distribution of the resistivity inside the body.

Also present in tissue are bound charges. In the presence of an electromagnetic field, these charges give rise to displacement currents that are manifested as phase shifts in the measured voltages relative to the applied currents. Phase shifts that vary from about 7° for lung to nearly 20° for cardiac muscle at an excitation frequency of 10 kHz have been reported [Schwan and Kay, 1957]. This ability of a material to store charge is referred to as its permittivity. Because the permittivity is related to the tissue type and is spatially variable, we can also consider producing an image of the permittivity distribution inside the body.

Some work suggests that these electrical characteristics are substantially altered in a variety

of pathological conditions. For instance, some investigators have demonstrated permittivity changes in excised malignant breast tumor specimens compared to normal tissue surrounding the tumor [Surowiec, *et al*, 1988]. Similarly, the non–invasive diagnosis and monitoring of pulmonary edema represents an attractive goal, since differences in the bulk resistivity properties of the lung may be detectable even with crude reconstruction algorithms [Isaacson, *et al*, 1990].

Biological Application of EIT

One of the first instruments designed to image the body's resistivity distribution was the "impedance camera" [Henderson and Webster, 1978]. This device consisted of one large electrode, positioned on the back, and an array of 144 electrodes, in a 12 by 12 grid, positioned on the chest, through which currents could be applied. In practice, measurements were made using 100 electrodes in an inner 10 by 10 grid, and currents were established on the outer "guard" electrodes in an attempt to "linearize" the current paths.

The authors monitored the current flow through each of the 100 measurement electrodes, and displayed iso–admittance curves on the body surface. They then proposed that reconstruction algorithms for the purpose of imaging the internal impedance should be developed.

Following this paper, many authors published descriptions of systems designed to reconstruct the impedance inside the body from electrical measurements made on the skin. Researchers began to apply mathematical tools developed for X-ray CT scanning to produce images of the body's internal impedance.

Investigators at the University of Sheffield [Barber, *et al*, 1983, Brown, *et al*, 1983] described a back–projection technique that was based on pre–computed equipotential lines in a homogeneous medium. In this technique, current was injected on two adjacent electrodes, and the resulting voltages were measured differentially on the remaining electrode pairs. The ratio of measured to predicted voltage was used to update the resistivity estimate in a strip between the isopotential lines ending on the measuring electrodes. This process was continued, with each electrode pair serving as the current injection electrodes.

More recently, these investigators have presented modifications to their original back–projection algorithm that uses a weighting system and logarithmic projection of the voltage ratios [Brown, *et al*, 1985]. Although strictly two dimensional, this algorithm is the basis for much of the *in-vivo* research in EIT.

In a 3–D body, current flow is not restricted to the plane of electrode placement, and the resistivity of tissues outside this plane contributes to errors in the Barber–Brown reconstruction scheme. Even in a 2–D body, current flow may be substantially perturbed by objects of varying resistivity.

In an attempt to address the problem of 3–D equipotential line distortion, a technique

that offers some improvement over the strictly 2–D algorithm has recently been described [Ider and Gencer, 1989, Ider, *et al*, 1990]. In this scheme, the authors compute an "equivalent translationally uniform" object that has the same equipotential lines as the three dimensional resistivity distribution. They used finite element techniques to compute modified 2–D equipotential lines by assuming that the resistivities obtained in the plane of electrode placement were translationally uniform. Other authors report experimental measurements of the sensitivity of back–projection reconstructors in 3–D domains [Guardo, *et al*, 1991].

Searching for more efficient algorithms, investigators have extended these techniques to the case of a cylinder with radial variations in conductivity [Andersen and Berntsen, 1988] and more recently, to a general formulation for the problem applicable to two and three–dimensional geometries [Berntsen, Andersen and Gross, 1991].

Other reconstruction techniques, including current path projection methods, "double constraint" techniques [Wexler, *et al*, 1985], and perturbation methods [Kim, *et al*, 1983] and [Tarassenko and Rolfe, 1984] have been applied to the EIT problem.

Iterative Newton's Method Techniques

Another approach to the solution of the inverse problem (and the one taken in this work) is the use of iterative linearization of the underlying nonlinear equations. This technique was suggested as early as 1978 [Lytle and Dines, 1978].

Later, these authors suggested an improved algorithm, using Newton's method to solve for each resistor in a 7x7 2–D array. This algorithm performed well on simulated data, even with the addition of 10 % additive noise [Dines and Lytle, 1981]. A patent [Bai, *et al*, 1984] appears to use a similar iterative technique.

Yorkey implemented an iterative algorithm using Newton's method. In his thesis, he compared the performance and computational costs associated with a variety of reconstruction algorithms of many reconstruction schemes, including the perturbation techniques [Kim, *et al*, 1983, Tarassenko and Rolfe, 1984], equi–potential back–projection techniques reminiscent of CT algorithms [Barber, *et al*, 1983, Barber and Brown, 1984] and double-constraint techniques [Wexler, *et al*, 1985]. He concluded that his "modified Newton--Raphson" was always the most accurate, at least on certain simulated data with and without added noise [Yorkey, 1986].

Simske implemented a two dimensional algorithm based on the Levenberg–Marquardt method using an analytic forward solver [Simske, 1987, Cheney, *et al*, 1990]. This method forms the basis for the extension of these concepts to three dimensions.

131

Mathematical Formulation of the Problem

Mathematically, the EIT problem can be formulated as follows:

Let $u(p)$ denote the electric potential at an arbitrary point p in Ω, a bounded domain in $\mathbf{R}^3$, and let $\sigma(p) = \frac{1}{\rho(p)}$ denote the conductivity at p. Then we assume that u satisfies

$$\nabla \cdot \sigma(p)\nabla u(p) = 0 \quad \text{for} \quad p \text{ in } \Omega. \tag{1}$$

We choose to solve the Neumann problem, so at the boundary, we have

$$\sigma(p)\frac{\partial u(p)}{\partial \nu} = j(p) \quad \text{on} \quad \partial\Omega \tag{2}$$

where ν denotes the unit outward normal and j denotes the current density applied on $\partial\Omega$. From conservation of charge , we require that

$$\int_{\partial\Omega} j(p) = 0. \tag{3}$$

To select a unique solution, we choose our reference potential so that

$$\int_{\partial\Omega} V(p) = 0, \tag{4}$$

where $V(p) = u(p)$ for p on $\partial\Omega$.

Notation for the 3–D Problem

Consider a right cylindrical volume with a three-dimensional electrode array on the surface, and with boundary conditions as in Figure 1. Let M denote the number of electrode planes and Λ denote the number of electrodes on any ring. Consequently, the total number of electrodes is $L = M\Lambda$. We denote an individual electrode by e_l, $l = 1, 2, 3, ..., L$.

Using external electronics, steady state patterns of current are established on the electrode array and measurements resulting from $L - 1$ orthogonal current patterns over the L electrodes are used to reconstruct the resistivity distribution within the object. Denote the kth applied current pattern by the L–vector I^k and the corresponding voltage measurement by another L-vector V^k, so that

$$I^k = \begin{bmatrix} I_1^k \\ I_2^k \\ I_3^k \\ \vdots \\ I_L^k \end{bmatrix} ; \qquad V^k = \begin{bmatrix} V_1^k \\ V_2^k \\ V_3^k \\ \vdots \\ V_L^k \end{bmatrix}. \tag{5}$$
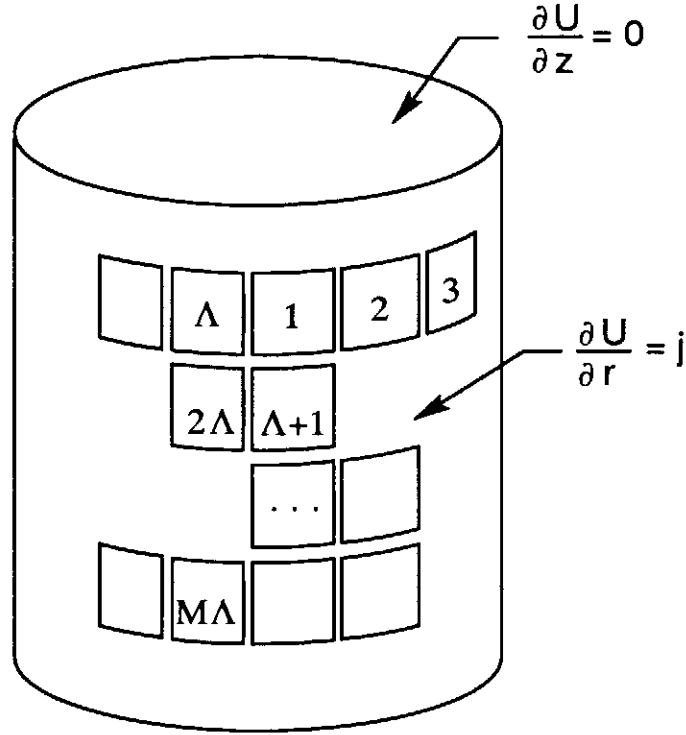
Figure 1: Nomenclature for the 3–D Problem

We will require a "reference" electrode, in order to enforce equation 4 . We may designate one electrode in the existing array, and simply measure all our voltages with respect to this electrode. Alternatively, we may supply an additional electrode which is tied directly to ground potential. We constrain each of the applied current patterns so that $\sum_{l=1}^{L} I_l = 0$, so that the current flowing through this ground electrode is negligible. To preserve this symmetry, we normalize the measured voltages so that $\sum_{l=1}^{L} V_l^k = 0$.

We define an operator $\mathbf{R}(\rho)$ that maps the applied current vector into the vector of measured voltages. We define another L-vector U^k

$$U^k = U(\rho) = \begin{bmatrix} U_1^k \\ U_2^k \\ U_3^k \\ \vdots \\ U_L^k \end{bmatrix} = \mathbf{R}(\rho) I^k \qquad (6)$$

which represents the predicted voltages on the electrodes due to some resistivity estimate ρ. The **forward problem** consists of predicting the voltages on L electrodes from knowledge (or an assumption) about the resistivity distribution inside the tank. In the case of a homogeneous cylinder, we can analytically solve for the predicted voltages U^k using a variety of models for the boundary conditions [Cheng, et al, 1990]. The more general case requires

use of finite difference or finite element techniques to solve the forward problem for an arbitrary resistivity distribution.

The **inverse problem** consists of predicting $\rho(p)$ throughout the body from knowledge of the applied currents and measured voltages. Because the operator $\mathbf{R}(\rho)$ is self–adjoint, we have at most

$$N_{max} = \frac{L(L-1)}{2} \tag{7}$$

degrees of freedom. Consequently, we subdivide the volume of interest into $N \leq N_{max}$ voxels, or volume elements, on which the resistivity is assumed constant. Hence we will compute a resistivity vector of length N such that

$$\rho(p) = \sum_{n=1}^{N} \rho_n \chi_n(p) \tag{8}$$

where

$$\chi_n(p) = \begin{cases} 1 & \text{if } p \text{ in voxel } n \\ 0 & \text{otherwise.} \end{cases} \tag{9}$$

We use ρ to denote the resistivity solution vector

$$\rho = \begin{bmatrix} \rho_1(p) \\ \rho_2(p) \\ \rho_3(p) \\ \vdots \\ \rho_N(p) \end{bmatrix}.$$

Figure 2 depicts the geometry of a typical voxel as used in our 3-D reconstructor.

Instrumentation Considerations

In this work, all experimental data was collected using **ACT IIB** , a 64 electrode system whose general design features have been described by Gisser *et al.* in 1987. This system is an improvement of the the original **ACT I** design to incorporate better voltmeter precision and phase stability [Fuks, 1989]. This instrument, which has subsequently been extended from 32 to 64 channel operation, can be used for 2-D or 3-D operation, depending on the software.

In operation, **ACT II** uses a Wein bridge one op–amp oscillator operating at about 15 kHz. Its amplitude is stabilized to better than 0.1 % by a DC feedback loop, and serves as a system–wide reference for amplitude and phase.

This primary frequency is fed simultaneously to 64 12 bit CMOS digital–to–analog converters, which act as digitally controlled attenuators for the master oscillator. This voltage
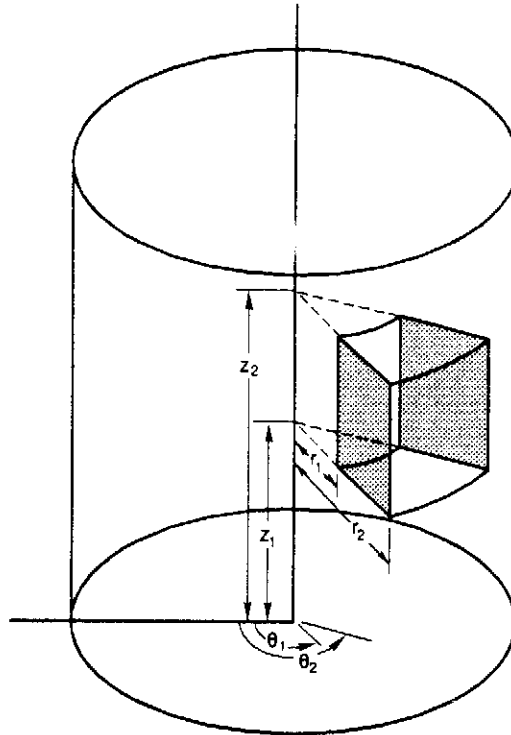
Figure 2: Geometry for the 3–D Resistivity Voxel

reference for each electrode is applied to op–amp voltage–to–current converters, and the resulting current is applied on the skin through shielded cables to the electrode.

The voltage required to maintain this fixed current flow will vary, depending on the resistivity of the object to be imaged. The voltage at the output of each current generator is fed through a 64:1 multiplexer into two demodulators synchronized to the master oscillator.

The first of these devices is synchronized by a signal that is in phase with the applied currents, and after rectification and low pass filtering, produces a DC signal proportional to the in–phase voltages on the electrodes. The second demodulator is synchronized with a signal that is $90°$ out of phase, producing a quadrature voltage related to the permittivity of the object. The resulting DC voltages are fed to a commercially available 16 bit analog–to–digital converter, a DT2801/5716 [1]. Table 2 is adapted from [Fuks, 1989].

A new instrument known as **ACT III** [Saulnier, et al, 1991] will incorporate a design philosophy similar to previous instruments but will exhibit substantially improved performance. Each electrode channel contains a digital signal processor (DSP), a current source, a voltmeter and associated amplifiers and calibration circuitry. These improvements will permit acquisition of all data, both in–phase and quadrature, with 16 bits of accuracy in 140 mSec.

---

[1]Data Translation, Inc., Marlborough, MA.

Characteristic	Specification
Oscillator	
Frequency	15.0 kHz
Frequency Stability	< 2 Hz
Amplitude Stability	< 0.1 %
Harmonic Distortion	< -60 dB
Waveform	Sinusoidal
Current Generators	
Number	64
Maximum Current	5 mA
Amplitude Precision	12 bits or 2.4 μA
Phase Coherence	0.3°
Voltmeter	
Type	Synch. Demodulation
Precision	16 bits (nominal)
Accuracy	10 ppm
Settling Time	1 ms for 12 bits
	3 ms for 16 bits
System Speed	
Write Time	
32 electrodes	0.55s
64 electrodes	0.95s
Read Time	
32 electrodes	0.38s
64 electrodes	0.80s
Total Image Time	
20 averages	390s

Table 2: **ACT II** Operational Specifications

A Least Squares 3–D Reconstruction Algorithm

The Plan

In our approach, the goal is to minimize the least square error functional $E(\rho)$,

$$E(\rho) = \sum_{k=1}^{L-1} ||V^k - U^k||^2 = \sum_{k=1}^{L-1} \sum_{l=1}^{L} (V_l^k - U_l^k)^2. \tag{10}$$

Here, V^k represents the voltages experimentally measured for the kth current pattern and U^k represents the predicted voltages for the same pattern. U^k is produced by the forward solver. It should be apparent that even if we have a perfect forward solver, and our initial estimate of the resistivity is uncannily correct, then our error function may not be equal to zero since the measured voltages V_l^k contain measurement errors. In fact, there may be no resistivity distribution $\rho(p)$ that produces the measured data!

We would like to improve our estimate ρ^0. We use Newton's method to compute a new estimate ρ^1. At a minimum,

$$0 = \frac{\partial E}{\partial \rho_n} = F_n(\rho) = -2 \sum_{k=1}^{L-1} \sum_{l=1}^{L} (V_l^k - U_l^k) \frac{\partial U_l^k}{\partial \rho_n}. \tag{11}$$

We then compute a new estimate,

$$\rho^{i+1} = \rho^i - [F'(\rho^i)]^{-1} F(\rho^i), \tag{12}$$

where

$$F'(\rho) = \begin{bmatrix} \frac{\partial F_1}{\partial \rho_1} & \cdots & \frac{\partial F_1}{\partial \rho_N} \\ \vdots & \ddots & \vdots \\ \frac{\partial F_N}{\partial \rho_1} & \cdots & \frac{\partial F_N}{\partial \rho_N} \end{bmatrix} \tag{13}$$

and

$$F'_{n,m}(\rho) = \frac{\partial F_m}{\partial \rho_n} = \frac{\partial^2 E}{\partial \rho_n \partial \rho_m} \tag{14}$$

$$= 2 \sum_{k=1}^{L-1} \sum_{l=1}^{L} \frac{\partial U_l^k}{\partial \rho_n} \frac{\partial U_l^k}{\partial \rho_m} - 2 \sum_{k=1}^{L-1} \sum_{l=1}^{L} (V_l^k - U_l^k) \frac{\partial^2 U_l^k}{\partial \rho_n \partial \rho_m}. \tag{15}$$

Regularization of F'

It would at first seem that finding ρ^{i+1} in equation 12 involves only inverting the known matrix, F', applying it to the vector F, and subtracting this term from the old resistivity estimate ρ^i. Unfortunately, F' is ill–conditioned [Simske, 1987].

137

Consider the first term of equation 13,

$$\mathbf{A}_{n,m} = 2\sum_{k=1}^{L-1}\sum_{l=1}^{L}\frac{\partial U_l^k}{\partial \rho_n}\frac{\partial U_l^k}{\partial \rho_m}. \tag{16}$$

We can think about this term as follows: If we apply the kth current pattern and calculate the voltage on the lth electrode, then perturb the resistivity on the nth voxel, then $\frac{\partial U_l^k}{\partial \rho_n}$ represents the voltage change. Similarly, $\frac{\partial U_l^k}{\partial \rho_m}$ represents the voltage change associated with a change in the resistivity on element m. If the mth and n^{th} voxels are in some sense "close" to each other, then the voltage changes they produce will be similar. Consequently, the product $\frac{\partial U_l^k}{\partial \rho_n}\frac{\partial U_l^k}{\partial \rho_m}$ will be large and positive.

Following a similar line of reasoning, we might presume that if the mth and n^{th} elements are quite remote, then the product $\frac{\partial U_l^k}{\partial \rho_n}\frac{\partial U_l^k}{\partial \rho_m}$ may likely be small. If the numbering of the elements is such that nearby elements have indices that are close together, then the matrix $\mathbf{A}$, whose elements are described by equation 16, will have its largest, positive elements on or near the diagonal.

The second term in equation 13,

$$\mathbf{B}_{n,m} = -2\sum_{k=1}^{L-1}\sum_{l=1}^{L}(V_l^k - U_l^k)\frac{\partial^2 U_l^k}{\partial \rho_n \partial \rho_m} \tag{17}$$

has no simple interpretation. But notice that if our estimate ρ is close to the true ρ, then this entire term will be close to zero. In this algorithm, we improve the condition of F' by neglecting the term $\mathbf{B}$ entirely, replacing it with

$$\mathbf{B}_{n,m} \approx \gamma \mathbf{A}_{n,m}\delta_{n,m}$$

where γ is a regularization parameter and $\delta_{n,m}$ is the Kroenecker delta. So

$$F'_{n,m} \approx \mathbf{A}_{n,m} + \gamma \mathbf{A}_{n,m}\delta_{n,m}. \tag{18}$$

The regularization parameter γ is chosen empirically to produce a balance between numerical stability and image contrast and definition. This well known regularization is used in the Levenberg–Marquardt method in, for example, [Press, et al, 1986].

Calculation of ρ^0

We now consider the problem of computing an initial resistivity estimate ρ^0 that is needed in equation 12. If we choose a uniform resistivity estimate, then we have

$$\rho^0 = \begin{bmatrix} \rho_1 \\ \rho_2 \\ \rho_3 \\ \vdots \\ \rho_N \end{bmatrix} = c \begin{bmatrix} 1 \\ 1 \\ 1 \\ \vdots \\ 1 \end{bmatrix}$$

where c is a scalar constant. We choose for the initial resistivity estimate ρ^0 the value that minimizes the error between the measured voltage values and the values predicted by the forward solver for a constant resistivity. Here, because the differential equation is linear, we can simplify

$$U_l^k(c\mathbf{1}) = cU_l^k(\mathbf{1}).$$

We would like to minimize

$$E(c\mathbf{1}) = \sum_{k=1}^{L-1} \sum_{l=1}^{L} \left[V_l^k - cU_l^k(\mathbf{1}) \right]^2. \tag{19}$$

Again, setting the derivative equal to zero, we have

$$\frac{\partial E}{\partial c} = -2 \sum_{k=1}^{L-1} \sum_{l=1}^{L} \left[V_l^k - cU_l^k(\mathbf{1}) \right] U_l^k(\mathbf{1}) = 0. \tag{20}$$

Now, we can solve for c to obtain

$$c = \frac{\sum_{k=1}^{L-1} \sum_{l=1}^{L} \left[V_l^k U_l^k(\mathbf{1}) \right]}{\sum_{k=1}^{L-1} \sum_{l=1}^{L} \left[U_l^k(\mathbf{1}) \right]^2}. \tag{21}$$

Thus we choose our initial guess so that $\rho^0 = c\mathbf{1}$, with c defined as in equation 21.

Computing $U_l^k(\rho^0)$

The next task is to predict the observed boundary voltages U_l^k for a homogeneous tank of resistivity ρ^0. We can solve this problem analytically. We have

$$\nabla^2 u = 0 \tag{22}$$

in the interior. The Neumann boundary conditions are

$$\frac{\partial u}{\partial z}(r, \theta, 0) = \frac{\partial u}{\partial z}(r, \theta, h) = 0 \tag{23}$$

on the top and bottom of the tank. On the sides of the tank,

$$\sigma^0 \frac{\partial u}{\partial r}(r_0, \theta, z) = j(\theta, z).$$ (24)

We assume that the current on the lth electrode is equal to the area of the electrode multiplied by $\sigma^0 \frac{\partial u}{\partial r}$ evaluated at the center of the electrode. Similarly, we assume that U_l^k, the voltage on the lth electrode, is just the potential u at the center of the lth electrode. These assumptions we refer to as the "continuum model" [Cheng, et al, 1990, Cheney, et al, 1990].

We can use separation of variables to solve

$$\nabla^2 u = u_{rr} + \frac{u_r}{r} + \frac{u_{\theta\theta}}{r^2} + u_{zz} = 0.$$ (25)

for the potentials on the boundary. We discover two sets of solutions. For $m = 0$ we find solutions that are constant in z:

$$U(r, \theta) = \frac{\rho^0 r_0}{n} \left(\frac{r}{r_0} \right)^n \cos(n\theta)$$ (26)

and

$$U(r, \theta) = \frac{\rho^0 r_0}{n} \left(\frac{r}{r_0} \right)^n \sin(n\theta)$$ (27)

For $m \neq 0$, we have solutions of the form:

$$U(r, \theta, z) = \frac{\rho^0 h}{m\pi} \frac{I_n\left(\frac{m\pi r}{h}\right)}{I_n'\left(\frac{m\pi r_0}{h}\right)} \cos(n\theta) \cos\left(\frac{m\pi z}{h}\right)$$ (28)

and

$$U(r, \theta, z) = \frac{\rho^0 h}{m\pi} \frac{I_n\left(\frac{m\pi r}{h}\right)}{I_n'\left(\frac{m\pi r_0}{h}\right)} \sin(n\theta) \cos\left(\frac{m\pi z}{h}\right).$$ (29)

where h is the height of the cylinder and $I_n(x)$ denotes the nth "modified Bessel function."

From these results, we can can write down characteristic current patterns for the 3–D problem in the test tank. These current patterns T^k satisfy $U_l^k = \rho_{m,n} T_l^k$, i.e., they are the eigenvectors of the operator $R(\rho^0)$ when ρ^0 is a constant.

These characteristic current patterns are the values at the electrode centers of

$$C \cos(n\theta) \cos\left(\frac{m\pi z}{h}\right), \quad \text{for} \quad m = 0, 1, ..., M-1; n = 1, 2, ..., \frac{\Lambda}{2}$$

$$C \sin(n\theta) \cos\left(\frac{m\pi z}{h}\right), \quad \text{for} \quad m = 0, 1, ..., M-1; n = 1, 2, ..., \frac{\Lambda}{2} - 1$$

$$C \cos\left(\frac{m\pi z}{h}\right), \quad \text{for} \quad m = 1, 2, ..., M-1; n = 0,$$ (30)

where C is the maximum amplitude available from our current generator electronics. We denote these characteristic patterns by $T^k, k = 1, 2, ..., \Lambda M - 1$. For instance, for a system with 4 rows of 16 electrodes, this defines a total of 63 orthogonal current patterns over the 64 electrodes.

Computing $\frac{\partial U^k(\rho^0)}{\partial \rho_n}$

From equation 12, we require the vector $\frac{\partial U^k(\rho^0)}{\partial \rho_n}$, and we can expand this vector in the orthogonal basis of equation 30:

$$\frac{\partial U^k(\rho^0)}{\partial \rho_n} = \sum_{s=1}^{L-1} \frac{<T^s, \frac{\partial U^k(\rho^0)}{\partial \rho_n}>}{<T^s, T^s>} T^s. \tag{31}$$

We show in [Cheney, et al, 1990] that

$$R^b_{s,k} = <T^s, \frac{\partial U^k(\rho^0)}{\partial \rho}> \approx \frac{1}{(\rho^0)^2} \int_{\text{voxel}_n} \nabla u^s \cdot \nabla u^k, \tag{32}$$

where u^α satisfies equations 22–24 and with the j of equation 24 corresponding to T^α.

Computation of these elements $R^b_{s,k}$ requires most of the computer time for the reconstruction. From equation 32, we see that these quantities depend only on the mesh geometry and can be precomputed. We demonstrate the computation for a typical 3-D integral below.

Typical R Matrix Calculation

We demonstrate a typical calculation for the R matrix elements. In total, there will be 25 such cases, related to the each type of current pattern from equation 30 with each of the other types of current patterns. Fortunately, the calculations are highly degenerate. We use the continuum model for all the derivative calculations. Consider the case where I^α is the vector composed of

$$c^\alpha \cos(n\theta) \cos\left(\frac{m\pi z}{h}\right) \tag{33}$$

evaluated at the center of the electrodes, and I^k corresponds in a similar way to

$$c^k \cos(n\theta) \cos\left(\frac{m\pi z}{h}\right). \tag{34}$$

The scalar c has been chosen so that $\sum_{l=1}^L (I_l^\alpha)^2 = 1$.

Using the "continuum" electrode model,

$$U^\alpha(r, \theta, z) = \frac{c^\alpha \rho^0 h}{m\pi} \frac{I_n\left(\frac{m\pi r}{h}\right)}{I'_n\left(\frac{m\pi r_0}{h}\right)} \cos(n\theta) \cos\left(\frac{m\pi z}{h}\right), \tag{35}$$

and U^k is governed by a similar equation. From equation 32, we have

$$R_{\alpha,k}^b = \frac{1}{(\rho^0)^2} \int_{\text{voxel}_b} \nabla u^\alpha \cdot \nabla u^k dv. \tag{36}$$

Substituting our expression for the potential yields

$$
\begin{aligned}
R_{\alpha,k}^b &= \frac{c^\alpha c^k h^2 (\rho^0)^2}{(\rho^0)^2 m^\alpha m^k \pi^2 I_{n^\alpha}\left(\frac{m^\alpha \pi r_0}{h}\right) I_{n^k}\left(\frac{m^k \pi r_0}{h}\right)} \\
&\quad \int_{\text{voxel}_b} \nabla\left[I_{n^\alpha}\left(\frac{m^\alpha \pi r}{h}\right) \cos(n^\alpha \theta) \cos\left(\frac{m^\alpha \pi z}{h}\right)\right] \cdot \\
&\quad \nabla\left[I_{n^k}\left(\frac{m^k \pi r}{h}\right) \cos(n^k \theta) \cos\left(\frac{m^k \pi z}{h}\right)\right]
\end{aligned} \tag{37}
$$

after constants are factored and removed from beneath the integral. Now we use the fact that in cylindrical coordinates,

$$\iiint \nabla u \cdot \nabla v = \int \frac{u_\theta v_\theta}{r^2} + \int u_r v_r + \int u_z v_z. \tag{38}$$

to carry out the integration in equation 37. The integral involving only the θ derivatives is

$$
\begin{aligned}
\int_{\text{voxel}_b} &\frac{I_{n^\alpha}\left(\frac{m^\alpha \pi r}{h}\right) I_{n^k}\left(\frac{m^k \pi r}{h}\right)}{r^2} \cos\left(\frac{m^\alpha \pi z}{h}\right) \cos\left(\frac{m^k \pi z}{h}\right) \\
&n^\alpha n^k \sin(n^\alpha \theta) \sin(n^k \theta) r \, dr \, d\theta \, dz,
\end{aligned} \tag{39}
$$

which is

$$
\begin{aligned}
n^\alpha n^k \int_{r_1}^{r_2} &\frac{I_{n^\alpha}\left(\frac{m^\alpha \pi r}{h}\right) I_{n^k}\left(\frac{m^k \pi r}{h}\right)}{r} dr \quad \int_{\theta_1}^{\theta_2} \sin(n^\alpha \theta) \sin(n^k \theta) d\theta \\
&\int_{z_1}^{z_2} \cos\left(\frac{m^\alpha \pi z}{h}\right) \cos\left(\frac{m^k \pi z}{h}\right) dz.
\end{aligned} \tag{40}
$$

Undaunted, we continue with the term involving only r derivatives of equation 38, finding

$$
\begin{aligned}
\frac{m^\alpha m^k \pi^2}{h^2} \int_{r_1}^{r_2} &I'_{n^\alpha}\left(\frac{m^\alpha \pi r}{h}\right) I'_{n^k}\left(\frac{m^k \pi r}{h}\right) r \, dr \quad \int_{\theta_1}^{\theta_2} \cos(n^\alpha \theta) \cos(n^k \theta) d\theta \\
&\int_{z_1}^{z_2} \cos\left(\frac{m^\alpha \pi z}{h}\right) \cos\left(\frac{m^k \pi z}{h}\right) dz.
\end{aligned} \tag{41}
$$

Finally, we turn our attention to the term involving z derivatives:

$$
\begin{aligned}
\frac{m^\alpha m^k \pi^2}{h^2} \int_{r_1}^{r_2} &I_{n^\alpha}\left(\frac{m^\alpha \pi r}{h}\right) I_{n^k}\left(\frac{m^k \pi r}{h}\right) r \, dr \quad \int_{\theta_1}^{\theta_2} \cos(n^\alpha \theta) \cos(n^k \theta) d\theta \\
&\int_{z_1}^{z_2} \sin\left(\frac{m^\alpha \pi z}{h}\right) \sin\left(\frac{m^k \pi z}{h}\right) dz.
\end{aligned} \tag{42}
$$

Computer	Operating System	CPU Utilization (seconds)
Sun 4/150	SunOS	285
IBM 3092 w/VF	AIX	16.2
Cray Y/MP	UNICOS	2.6

Table 3: Some Typical Run Times for *N3D*

We find that if *both* patterns are of the form of equation 33, then equations 40-42 provide an expression for $R_{\alpha,k}$ for voxel b. We (or at least *Mathematica*[2]) can analytically integrate the terms involving only sine and cosine, but terms containing the modified Bessel functions I and their derivatives I' must be evaluated numerically. Here, these integrations are performed using Simpson's rule.

Expressions similar to equations 40-42 can be worked out for other combinations of current patterns.

Images from *N3D*

N3D has been implemented in FORTRAN for a cylindrical domain. In this section, we demonstrate images from *N3D* using experimentally obtained voltage data. Typical execution times for several machines are displayed in Table 3 for a problem with 420 degrees of freedom.

Figure 3 demonstrates a test configuration consisting of a tank, 30 cm in diameter and 26 cm high. This tank was filled with saline adjusted to approximately 900 $\Omega - cm$. The cylinder's wall was lined with 64 electrodes, arranged as 4 rows of 16 electrodes per row. The electrodes consisted of stainless steel about 5 cm square, shaped to conform to the tank inner surface. Also indicated in the figure is the discretization of the domain into 420 resistivity voxels.

Two objects were introduced into this volume. The first object consisted of a cylinder of copper, 3.3 cm in diameter and 5 cm high. It was placed at the level of the third electrode plane. The second target was a teflon cylinder, 3.3 cm in diameter and 13 cm high, placed so that it was confined to the topmost and second electrode planes.

Currents in several configurations were applied to the test tank. The first experiment was designed to simulate two–dimensional acquisition in the three–dimensional volume. Here, an orthogonal set of currents were applied on the third plane of electrodes, and the resulting

---

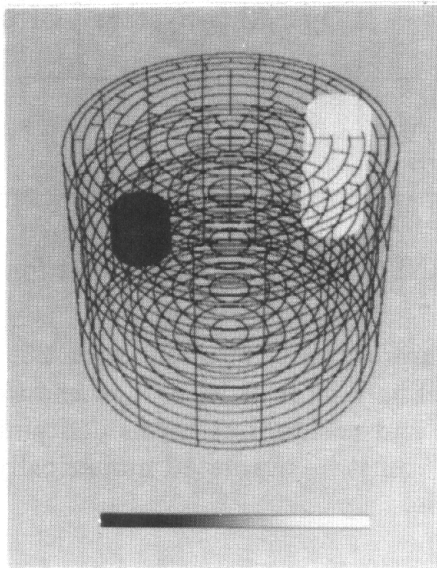[2]Wolfram Research, Inc., Champaign, IL.
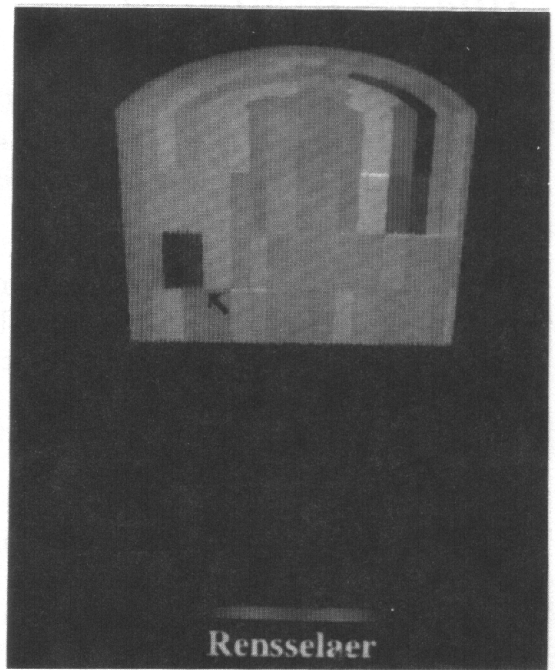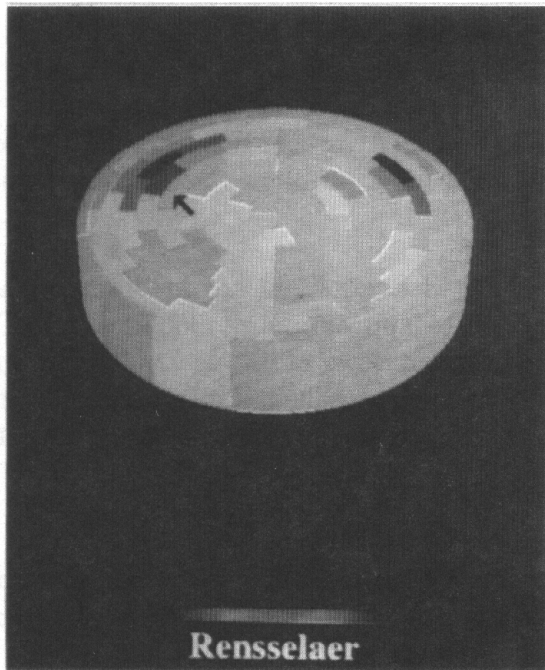
Figure 3: Test Tank Configuration

Figure 4: *NOSER* Reconstruction (l.) and *N3D* Reconstruction (r.)

voltages were used to reconstruct the resistivity distribution in the plane using a sixteen electrode variation of the 2–D *NOSER* code [Cheney, *et al*, 1990]. The targets were removed from the tank, an appropriate volume of saline added to replenish the displaced volume of the targets, and a second set of voltages were acquired. This "background" data was also reconstructed using the *NOSER* code. Resistivity reconstructions with and without the targets were subtracted, and the resulting net resistivity vector was processed using 3–D visualization software.

The resulting image, displayed on the left in Figure 4, clearly demonstrates the presence of the conductive target. However, an artifact of increased resistivity also appears in the image in an area that underlies the position of the resistive cylinder. The net resistivity of this reconstruction ranges from -4.2 to +2.1 $\Omega - cm$. The presence in the image of resistivity perturbations outside the plane of the electrodes demonstrates the importance of truly three–dimensional reconstruction algorithms.

To demonstrate the improved performance of *N3D*, the canonical current patterns T^k were scaled to 5 mA and established on the electrode array. Again, the resistivity vector resulting from the *N3D* reconstruction and the "background" vector were subtracted to produce a net resistivity image. This image, displayed as a three–dimensional cylinder cut away through the plane of the targets to reveal the resistivity reconstruction in the interior, demonstrates the ability of the algorithm to obtain information about the resistivity distribution along the longitudinal axis of the cylinder. The net resistivity image displayed on the right in Figure 4 ranges from -9.7 to +14.3 $\Omega - cm$.

References

[Andersen and Berntsen, 1988] J. B. Andersen and S. Bernsten Quasi-static profile reconstruction of a circular cylinder. *Journal of Electromagnetic Waves and Appl*, 2:429-444, 1988.

[Bai, *et al*, 1984] D. Bai, A. E. Brandt, and B. D. Sollish. Apparatus and techniques for electric tomography, 1984. U.S. Patent 4,486,835.

[Baker, 1989] Lee E. Baker. Principles of the impedance technique. *IEEE Engineering in Medicine and Biology*, 3(5):11–15, 1989.

[Barber and Brown, 1984] D. C. Barber and B. H. Brown. Applied potential tomography. *Journal of Physics E: Scientific Instrumentation*, 17:723–733, 1984.

[Barber, *et al*, 1983] D. C. Barber, B. H. Brown, and I. L. Freeston. Imaging spatial distributions of resistivity using applied potential tomography. *Electronic Letters*, 19:933–935, 1983.

[Berntsen, Andersen and Gross, 1991] S. Bernsten, J. B. Andersen and E. Gross. A general formulation of applied potential tomography. *Radio Science*, 26:535-540, 1991.

[Brown, *et al*, 1983] B. H. Brown, D. C. Barber, and I. L. Freeston. Potential tomography, 1983. U.K. Patent 2119520.

[Brown, *et al*, 1985] B.H. Brown, D.C. Barber, and A.D. Seager. Applied potential tomography: Possible clinical applications. *Clinical Physics and Physiological Measurement*, 6(Supplement A):109–121, 1985.

[Cheney, *et al*, 1990] M. Cheney, D. Isaacson, J. C. Newell, S. Simske, and J. Goble. NOSER: An algorithm for solving the inverse conductivity problem. *International Journal of Imaging Systems and Technology*, 2:66–75, 1990.

[Cheng, *et al*, 1990] Kuo–sheng Cheng, D. Isaacson, J. C. Newell, and D. G. Gisser. Electrode models for electric current computed tomography. *IEEE Transactions on Biomedical Engineering*, 37(1):60–65, 1990.

[Dines and Lytle, 1981] K. A. Dines and R. J. Lytle. Analysis of electrical conductivity imaging. *Geophysics*, 46:1025–1036, 1981.

[Fuks, 1989] Luiz Felipe Fuks. *Reactive Effects in Impedance Imaging*. PhD thesis, Rensselaer Polytechnic Institute, Troy, NY, 1989.

[Fry and Wexler, 1985] B. Fry and A. Wexler. Reconstruction system and methods for impedance imaging, 1985. U.S. Patent 4,539,640.

[Goble, 1990] John C. Goble. *The Three-Dimensional Inverse Problem in Electric Current Tomography*. PhD thesis, Rensselaer Polytechnic Institute, Troy, NY, 1990.

[Guardo, *et al*, 1991] R. Guardo, C.Boulay, B. Murray, and M. Bertrand. An experimental study in electrical impedance tomograpy using backprojection reconstruction. *IEEE Transactions on Biomedical Engineering*, 38:617–627, 1991.

[Henderson and Webster, 1978] R. P. Henderson and J. G. Webster. An impedance camera for spatially specific measurements of the thorax. *IEEE Transactions on Biomedical Engineering*, 27:250–254, 1978.

[Ider and Gencer, 1989] Y. Ziya Ider and Nevzat G. Gencer. An algorithm for compensating for 3d effects in electrical impedance tomography. *Proceedings, IEEE Engineering in Medicine and Biology*, 2:465–466, 1989.

[Ider, *et al*, 1990] Y. Ziya Ider, Nevzat G. Gencer, Ergin Atalar, and Haluk Tosun. Electrical impedance tomography of translationally uniform cylindrical objects with general cross–sectional boundaries. *IEEE Transactions on Medical Imaging*, 9(1):49–59, 1990.

[Isaacson, *et al*, 1990] D. Isaacson, J.C. Newell, J.C. Goble and M. Cheney. Thoracic impedance images during ventilation. *Proceedings, IEEE Engineering in Medicine and Biology*, 12(1):106–107, 1990.

[Kim, *et al*, 1983] Y. Kim, J.G. Webster, and W.J. Tompkins. Electrical impedance imaging of the thorax. *Journal of Microwave Power*, 18:245–257, 1983.

[Lytle and Dines, 1978] R. J. Lytle and K. A. Dines. An impedance camera: A system for determining electrical conductivity. *Lawrence Livermore Laboratories*, (UCRL–52413), 1978.

[Press, *et al*, 1986] W.H. Press, B.P. Flannery, S.A. Teukolsky and W.T.Vetterling. *Numerical Recipes: The Art of Scientific Computing*, Cambridge, New York, 1986.

[Saulnier, *et al*, 1991] G. Saulnier, R.D. Cook, D.G. Gisser, J.C. Goble, C.G. Hochgraf, D. Isaacson and J.C. Newell. A high–speed, high–precision electrical impedance tomograph. *Proceedings, IEEE Engineering in Medicine and Biology*, 1:5–6, 1991.

[Schwan and Kay, 1957] H. P. Schwan and C. F. Kay. The conductivity of living tissues. *Annals of the New York Academy of Science*, 65:1007–1013, 1957.

[Simske, 1987] Steven J. Simske. An adaptive current determination and a one-step reconstruction technique for a current tomography system. Master's thesis, Rensselaer Polytechnic Institute, Troy, NY, 1987.

[Surowiec, *et al*, 1988] A.J. Surowiec, S.S. Stuchly, J. R. Barr, and A. Swarup. Dielectric properties of breast carcinoma and the surrounding tissues. *IEEE Transactions on Biomedical Engineering*, 35(4):257–263, 1988.

[Tarassenko and Rolfe, 1984] L. Tarassenko and P. Rolfe. Imaging spatial distributions of resistivity– an alternative approach. *Electronic Letters*, 20:574–576, 1984.

[Wexler, *et al*, 1985] Alvin Wexler, B. Fry, and M. R. Neuman. Impedance-computed tomography algorithm and system. *Applied Optics*, 24:3985–3992, 1985.

[Yorkey, 1986] Thomas J. Yorkey. *Comparing Reconstruction Methods for Electrical Impedance Tomography*. PhD thesis, University of Wisconsin - Madison, Madison, WI, 1986.

Acknowlegements